Sensors and Actuators Reports 8 (2024) 100218

Contents lists available at ScienceDirect

Sensors and Actuators Reports

journal homepage: www.sciencedirect.com/journal/sensors-and-actuators-reports

Prussian blue nanofilm-sensitized plasmonic electrochemical microscopy for spatially resolved detection of the localized delivery of hydrogen peroxide

Adaly Garcia, Christina Dhoj, Samuel Groysman, Kinsley Wang, Stellina Ao, Aimee Anguiano, Tony Tran, Dianlu Jiang, Yixian Wang *

Department of Chemistry and Biochemistry, California State University, Los Angeles, Los Angeles, CA, USA

ARTICLE INFO

Keywords:
Prussian blue
Electrochemistry
Hydrogen peroxide sensing
Surface plasmon resonance
Dye-sensitized imaging
Numerical simulations

ABSTRACT

Hydrogen peroxide (H_2O_2) sensing has been widely investigated using various electrochemical methods, yet the challenge of finding an imaging technique capable of real-time, spatially resolved detection remains. Addressing this, we introduce a Prussian blue (PB) nanofilm-sensitized plasmonic electrochemical microscopy (PEM) technique that successfully visualizes the localized delivery of H_2O_2. The PB nanofilm was carefully characterized, and its sensing capability towards H_2O_2 was demonstrated in amperometric mode. Employing a precise micromanipulator system, we controlled a micropipette to create a localized concentration gradient on the sensor surface and monitored the gradient through the PB nanofilm-sensitized PEM. The accuracy of the obtained concentration values was further validated by numerical simulations based on finite-element methods. Our technique ensures dependable localized detection, and we anticipate that advancements in film uniformity will further improve the resolution. The potential applications of this technique are broad and significant, including the opportunity to investigate single-cell exocytosis with neurotransmitters like dopamine, thus offering a promising avenue for future biomedical research.

1. Introduction

Traditional electrochemical (EC) techniques typically quantify averaged responses from a collection of individual elements, encompassing microstructures, mesoscopic substances, ions, and molecules [1]. Such approaches, while effective for bulk analysis, often overlook the complex heterogeneity inherent in many systems. This limitation underscores the imperative need for developing EC methodologies that can achieve spatially resolved detection. Advancements in this domain have led to an array of scanning probe-based imaging methods—such as scanning electrochemical microscopy (SECM) [2,3] and scanning electrochemical cell microscopy (SECCM) [4,5]—as well as adapting optical techniques such as fluorescence [6], plasmonic [7], dark field [8], and Raman scattering microscopy [9]. While scanning probe techniques offer greater spatial resolution, their temporal resolution is less optimal. Optical methods, conversely, deliver high temporal resolution with the trade-off of diminished spatial information. Within this spectrum of tools, plasmonic electrochemical microscopy (PEM) emerges as a powerful technique, employing surface plasmon resonance (SPR) [10] on metallic nanofilm electrodes (e.g., Au or Ag) to enable spatially resolved detection at scales previously unattainable with conventional EC approaches [11-13]. PEM records local changes due to the EC processes on the electrode, in which the plasmonic signals are associated with redox reaction-induced bulk refractive index changes near the metal film, dielectric property changes of the metal film (e.g. surface charge density), redox molecular binding, or EC-induced deposition of an extra layer onto the metal film [14-17]. The microscopy feature of PEM enables spatially resolved analysis of the electrochemical activities on the electrode surface [12,13,18-22].

We present a novel advancement in PEM with the introduction of a "dye-sensitized" approach, designated as DS-PEM. This technique innovatively employs a redox-active dye coating on the PEM sensor, significantly boosting sensitivity while maintaining precise spatial resolution. The underlying concept leverages the dye's color change during specific electrochemical reactions to generate intensified optical signals detectable by PEM. Our model application for this enhanced method is

* Corresponding author at: Department of Chemistry and Biochemistry, California State University, Los Angeles, Los Angeles, CA, USA.
E-mail address: ywang184@calstatela.edu (Y. Wang).

https://doi.org/10.1016/j.snr.2024.100218
Received 10 April 2024; Received in revised form 10 June 2024; Accepted 14 June 2024
Available online 26 June 2024

the detection of hydrogen peroxide (H_2O_2), a reactive oxygen species with pivotal roles in various physiological processes and an established biomarker in health diagnostics [23-25]. Conventional electrochemical assays—such as amperometry, voltammetry, and impedance spectroscopy—remain prevalent for H_2O_2 detection but often fall short in spatial resolution. Previously reported spatially resolved detection techniques, including microsensor arrays [26], SECM [27], and fluorescent imaging [28,29], encounter challenges such as low throughput, laborious protocols and dependence on fluorescent labeling.

The DS-PEM strategy addresses these challenges by utilizing a Prussian blue (PB) nanofilm as a sensing layer on the PEM sensing chip, building on our earlier work demonstrating that Prussian blue nanoparticles (PBNPs) enable H_2O_2 detection via catalytic reduction [21]. In the absence of H_2O_2, PB can be electrochemically reduced to Prussian white (PW), which generates a detectable increase in the PEM signal due to the refractive index change. In the presence of H_2O_2, some of the reduced form, PW, catalytically reduces H_2O_2 and converts back to PB. This reduces the overall amount of conversion from PB to PW, causing a smaller refractive index change and a smaller increase in PEM signal. As a result, the PEM signal can be inversely correlated with H_2O_2 levels—a phenomenon that enables us to establish a negative linear feedback relationship. In the current work, we apply a uniform layer to the PEM sensor that enables the sensitive detection of H_2O_2 in a spatially resolved manner. The deposition of a PB film was conducted through the modification of a reported procedure [30] and then applied to test the plasmonic response. By delivering H_2O_2 via a micropipette, we simulated a controlled release scenario, reflecting the localized concentration changes that are critical in biological and environmental processes. Through our DS-PEM approach, we successfully mapped these microscale H_2O_2 distributions, with the fidelity of our detection confirmed by numerical simulations based on finite-element methods. These simulations provided a robust validation of our technique, cementing DS-PEM's potential as a pivotal tool for precise, spatially resolved electrochemical analysis.

2. Experimental section

2.1. Chemicals and materials

Ferric chloride, hydrochloric acid, hydrogen peroxide (3% w/v), potassium chloride, potassium ferricyanide, potassium ferrocyanide, and potassium nitrate were purchased from Fisher Scientific (Waltham, MA, United States) and used without further purification. All aqueous solutions were prepared using double-deionized water (resistivity = 18.2 MΩ·cm at 25 °C, Milli-Q Ultrapure water EQ 7000 Purification System, MilliporeSigma, Burlington, MA, United States). Silicon wells were cut from flexiPERM re-usable silicon inserts (Sarstedt, Germany). The electrodes, including the sensing chips (18 mm × 18 mm, glass coverslips coated with a 2 nm titanium layer and a 50 nm gold layer, also used as working electrodes), Ag/AgCl (1 M KCl) reference electrodes, and Pt wire counter electrodes were purchased from Biosensing Instruments (Tempe, AZ, United States).

2.2. Preparation and characterization of the Prussian blue nanofilm

The PB nanofilm was fabricated by depositing synthesized PBNPs onto sensing chips, with subsequent annealing to form a fully integrated sensing interface [30]. The PBNPs were prepared by stirring equimolar solutions of 2 mM potassium ferrocyanide and ferric chloride in a mixture containing 0.1 mM potassium chloride and 10 mM hydrochloric acid for 12 h [31,32]. The as-prepared PBNPs were applied to the sensing chips within one week to maintain their chemical activity.

The gold chips were thoroughly cleaned with three sequential washes of water and ethanol, dried with nitrogen gas, and then annealed with hydrogen gas for 30 s to remove residual impurities. A clean silicon well was subsequently attached to the chip to contain the PBNPs solution, and the mixture was left to sit overnight to secure even coverage. Following the deposition, the solution was removed, and the chip was dried with nitrogen gas and then baked at 100 °C overnight [30,33]. This process annealed the PBNPs into a nanofilm.

The surface morphology of the prepared chips was analyzed using atomic force microscopy (AFM). This analysis was performed in non-contact air mode employing a Park NX12 multifunctional microscopy platform (Park Systems, Seoul, South Korea), which features a detachable AFM head and is equipped with non-contact cantilevers (PPP-NCHR, 42 N/m, 330 kHz). The instrument was operated with the Smart Scan software, and the captured AFM images were processed using the XEI software, both provided by Park Systems, Seoul, South Korea. All images were first-order flattened before the surface roughness was determined as the root-mean-square deviation of z-heights across the surface in sections of 1 μm × 1 μm.

The chemical composition of the PB film-coated sensors was validated by scanning electron microscopy with energy-dispersive X-ray spectroscopy (SEM-EDS) using the Axia ChemiSEM system equipped with a TrueSight EDS detector (Thermo Fisher Scientific, Waltham, MA., USA). Additionally, the films underwent analysis by attenuated total reflectance Fourier transform infrared spectroscopy (ATR-FTIR) using a Thermo Nicolet 6700 FT-IR spectrometer with the Smart Orbit ATR accessory operated via OMNIC software (Thermo Fisher Scientific, Waltham, MA., USA).

2.3. Instrument setup

PEM experiments were conducted using a surface plasmon resonance microscopy system (SPRm 200 Series, Biosensing Instruments, Tempe, AZ, USA) integrated with a potentiostat (CHI760E, CH Instruments, Austin, TX, USA) for synchronized electrochemical measurements. As illustrated in Scheme 1, the electrochemical cell was housed in a silicon well on the sensing chip and filled with a 1 M KNO_3 electrolyte. A conventional three-electrode system comprised of a Ag/AgCl (1 M KCl) reference electrode, a platinum wire counter electrode, and the sensing chip as the working electrode with an approximate surface area of 0.9 cm^2 was employed.

The EC cell was mounted onto the prism stage with a refractive index matching fluid. P-polarized light was directed onto the gold chip through the prism to induce plasmonic excitations, and variations in the reflected light intensity were captured by an SPR detector. The potentiostat was used to induce electrochemical reactions, with the PEM system capturing image sequences and the potentiostat recording conventional electrochemical signals in parallel. Operation of the PEM system was managed using ImageSPR software (Biosensing Instruments, Tempe, AZ, USA), and both cyclic voltammetry and amperometry were conducted via the potentiostat. The voltammograms presented are of the first cycle.

For spatially resolved sensing experiments, the PEM setup was operated under a constant potential bias while H_2O_2 was locally delivered to the sensing chip using a micropipette controlled by a 3-Axis Micromanipulator System (TRIO/MP-245A, Sutter Instrument, Novato, CA, USA) and a head stage (Axon Instrument, CV 203BU Molecular Device, San Jose, CA, USA). Micropipettes with a tip diameter of approximately 10 μm were pulled from quartz capillaries (with filament, 1.0 mm O.D., 0.5 mm I.D., 7.5 cm length) using a P-2000 laser puller (Sutter Instrument, Novato, CA, USA). The parameters were set to Heat = 500, Filament = 3, Velocity = 16, Delay = 120, and Pull = 45. The quartz micropipettes, filled with an 88 μM solution of hydrogen peroxide, were cautiously approached toward the sensing chip. The position of the micropipette was continuously monitored in real-time. To determine the distance between the pipette and the substrate, we carefully lowered the pipette tip until it made gentle contact with the substrate. Contact was confirmed by the appearance of a new tail in the SPR image. The z-value at the moment of contact is designated as zero for all subsequent measurements. Following contact, the tip was

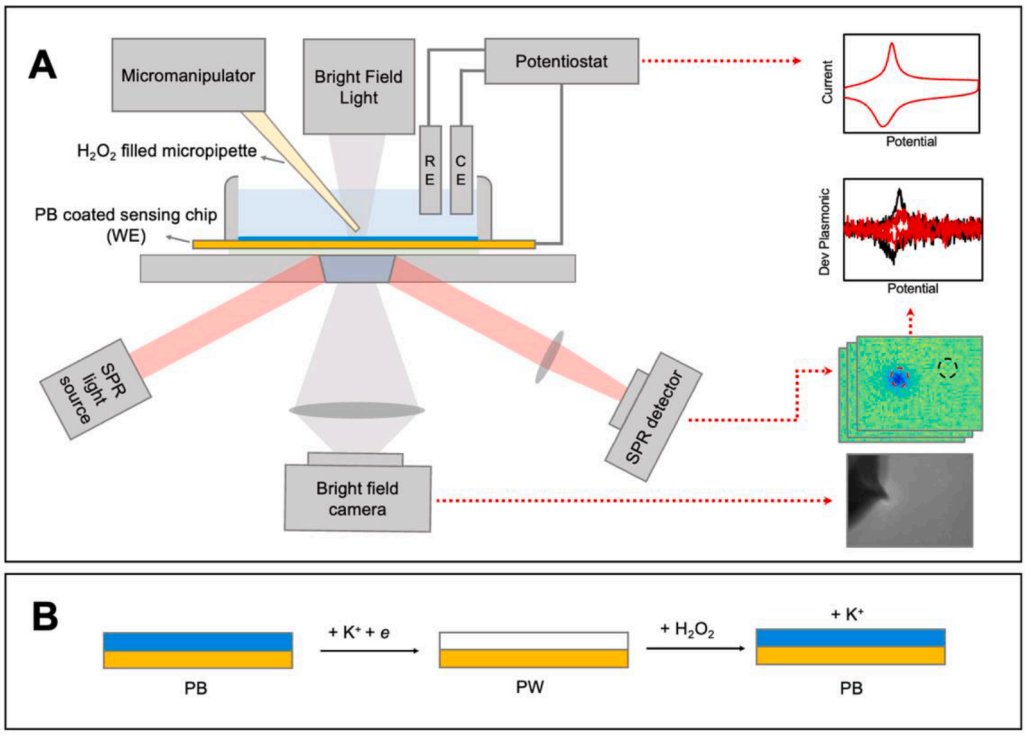

Scheme 1. (A) Schematic of the DS-PEM setup and corresponding data visualization; (B) Reaction mechanism at the PB film.

promptly retracted, and the sensing region was relocated to ensure that the surface interaction did not influence subsequent measurements. While there might be minor pipette damage during this process, it does not compromise our experimental assumptions, as the pipette is solely employed as a localized source of H_2O_2. Although precise distance control can be potentially achieved without risk of collision using scanning ion conductance microscopy [34], such refinement falls outside the scope of the present study.

2.4. Data processing

Raw plasmonic image stacks were converted to .tif image sequences using ImageAnalysis (Biosensing Instruments, Tempe, AZ, United States). Plasmonic data were then extracted at specific locations from these image sequences using ImageJ 1.53c (Wayne Rasband, National Institutes of Health, United States) and further processed in Excel. Alternatively, the image sequences were processed with imaging processing algorithms implemented with MATLAB (R2019b; MathWorks). In amperometry tests where a constant bias was applied, the data was background (first frame) subtracted and normalized to a percentage response, calculated as (plasmonic signal / 65,536) × 100%, with 65,536 representing the full scale of intensity units. For cyclic voltammetry tests, we calculated the first order derivative over time and presented the data in arbitrary units (a.u.). It is important to note that we did not calibrate the plasmonic signals in the PEM images to correspond to actual local current density values. Instead, our conclusions are drawn from the relative intensities of the plasmonic signals within the same sample.

2.5. Numeric simulations

Numeric simulations were run in COMSOL Multiphysics 6.0 using the "transport of diluted species" module. To approximate the concentration gradient inside the pipette arising from being kept in solution before approaching the gold chip, we first simulated H_2O_2 diffusion from the pipette for 1 min. We then used the resulting concentration gradient within the pipette to simulate H_2O_2 diffusion to the electrode surface at varying distances. The diffusion coefficient for H_2O_2 was taken from literature [35]. A complete COMSOL report has been provided in the supporting information.

3. Results and discussions

3.1. Characterization of Prussian blue nanofilms

The chemical and physical properties of the nanofilm-coated chips are depicted in Fig. 1. SEM-EDS images (Figs. 1A–C) reveal the elemental presence of carbon, iron, and nitrogen throughout the PB thin film, confirming the characteristic elemental features of PB, which consists of ferric and ferrous ions bridged by cyanide groups. The FTIR spectrum exhibits a sharp band at 2075 cm^{-1} (indicated in red in Fig. 1G), corresponding to cyanide stretching vibrations (C≡N), as previously reported [33,36]. This feature stands in contrast to the flat baseline spectrum (displayed in black) from an uncoated sensing chip in the same frequency range. The surface roughness and thickness of the PB nanofilm were quantified utilizing non-contact mode AFM. As illustrated in Figs. 1D and E, the surface of the PB coating exhibits a roughness value of 9.1 ± 0.9 nm, which is an increase compared to the 1.02 ± 0.02 nm roughness of the bare gold surface. At the interface where the PB nanofilm meets the bare chip, the film's thickness was consistently measured (Fig. 1F), yielding an average value of 26 ± 3 nm.

We evaluated the electrochemical performance of the sensing chip through cyclic voltammetry (CV). Fig. 1H represents the CV profiles obtained from the potentiostat for the sensing chip coated with the PB nanofilm (red) versus the uncoated chip (black). The coated chip's CV signature demonstrates the anticipated electrochemical behavior, indicative of the redox transitions between PB and PW as well as the potassium ion intercalation and deintercalation associated with these processes. The plasmonic CV of the PB nanofilm, shown in Fig. 1I (red), was derived by averaging plasmonic signals across the entire sensing surface area of 0.27 mm^2 (600 μm by 450 μm). This plasmonic CV closely matches the electrochemical CV from the potentiostat (Fig. 1H,

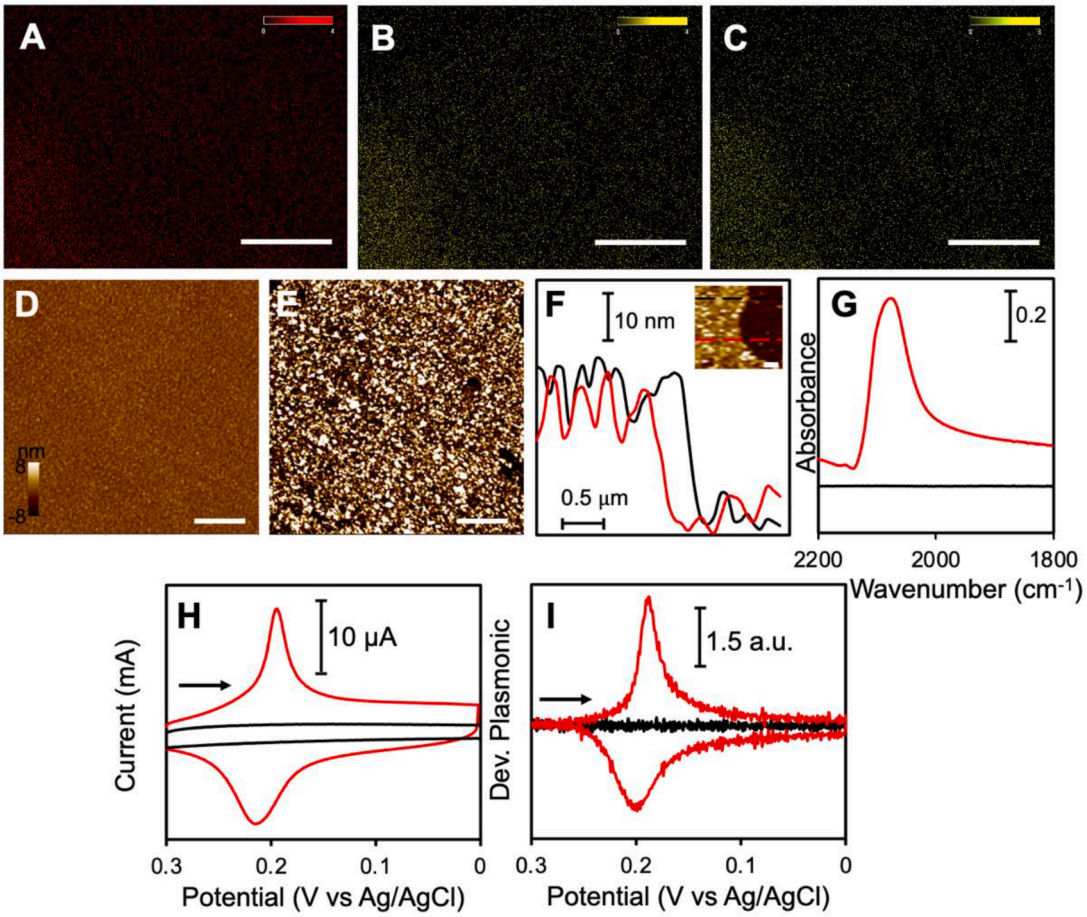

Fig. 1. Comprehensive Characterization of PB Nanofilm on a Sensing Chip. (A-C) SEM-EDS elemental mapping for carbon (A), iron (B), and nitrogen (C), affirming the chemical composition of the nanofilm. (D-F) AFM imaging comparing a bare sensing chip (D) with a PB nanofilm-coated chip (E), along with height profiles (F) taken at the nanofilm's boundary. Scale bars = 1 μm for A-E and 0.5 μm for F. All images were processed with first-order flattening via XEI. The inset in (F) illustrates the height profile extraction points, denoted by red and black dashed lines, with an average film height determined to be 26 ± 3 nm from three separate measurements. (G) ATR-FTIR spectra comparing the PB nanofilm (red) and bare chip (black), highlighting the characteristic peak at 2075 cm^{-1} for the cyanide group. (H, I) Electrochemical analysis of the PB-coated PEM chip as shown by: potentiostat cyclic voltammograms (CVs) from the whole electrode (~0.9 cm^2) (H) and plasmonic CVs averaged from the whole sensing area (600 μm × 450 μm, 0.27 mm^2) (I) for the PB-modified chip (red) versus the bare chip (black) collected at a scan rate of 0.05 V/s in a 1 M KNO_3 solution.

red), displaying corresponding redox peaks with minimal influence from capacitive charging. This suggests a high selectivity for Faradaic processes with our present setup. Conversely, the bare sensing chip (Fig. 1I, black) exhibited only minimal signal variation, aligning with the negligible current signal observed. In subsequent amperometric tests, a bias of −0.1 V was applied to maintain the sensing surface in the PW state.

3.2. Sensing capability of PB nanofilm-sensitized PEM

For H_2O_2 sensing, we applied a constant potential and monitored the current and plasmonic signals in response to various H_2O_2 concentrations. Fig. 2A–D show four representative snapshots of the PEM images during amperometry, correlating with sequential H_2O_2 injections. These snapshots exhibit a noticeable trend: a decrease in intensity with higher H_2O_2 concentrations, indicative of the catalytic reduction of H_2O_2 accompanying the conversion from PW to PB. A video of the whole process has been attached in the supporting information (Video 1). Fig. 2F presents the cumulative plasmonic signal from twelve injections averaged across the sensing area, further illustrating the plasmonic signal's concentration dependence. In contrast, the potentiostat current recordings shown in Fig. 2E displayed difficulty reaching plateau current after each injection and lacked concentration dependence toward higher concentrations.

We then extracted plasmonic signals from 88 regions of interest (ROIs, see Fig. S1 for ROI distribution), each measuring approximately 54 μm by 54 μm. Twelve data points were extracted for each ROI, corresponding to the twelve accumulative concentrations after each injection. Each data point was extracted right before the next injection to ensure reaching plateau values. The calibration curve derived from these ROIs' averaged signals (Fig. 2G) demonstrates a strong linear relationship with an R^2 value of 0.997 and a slope of −0.0355% Response/μM. Notably, a separate trial on a different chip yielded a slope of −0.0343% Response/μM (Fig. S2, Video 2), a mere 3.4% variation from the current trial (see Fig. S3 for the comparison of the SPR angles of the two sensors and more detailed discussion). This consistency validates the use of PEM signals to calculate H_2O_2 concentrations in the following localized detection experiments. Conversely, signals from bare sensing chips were markedly diminished (Fig. 2H–J), with the current change more than 10 times lower. The PEM signals were also notably weaker and more prone to fluctuation, leading to a less reliable calibration curve as evidenced by the lower R^2 value of 0.3403.

Some tails observed in the PEM snapshots and videos are likely due to the temporary binding of impurity particles introduced during the injections. Most of these impurities disappeared during the experiment. An example of a temporary binding event is shown in Fig. S4, in which

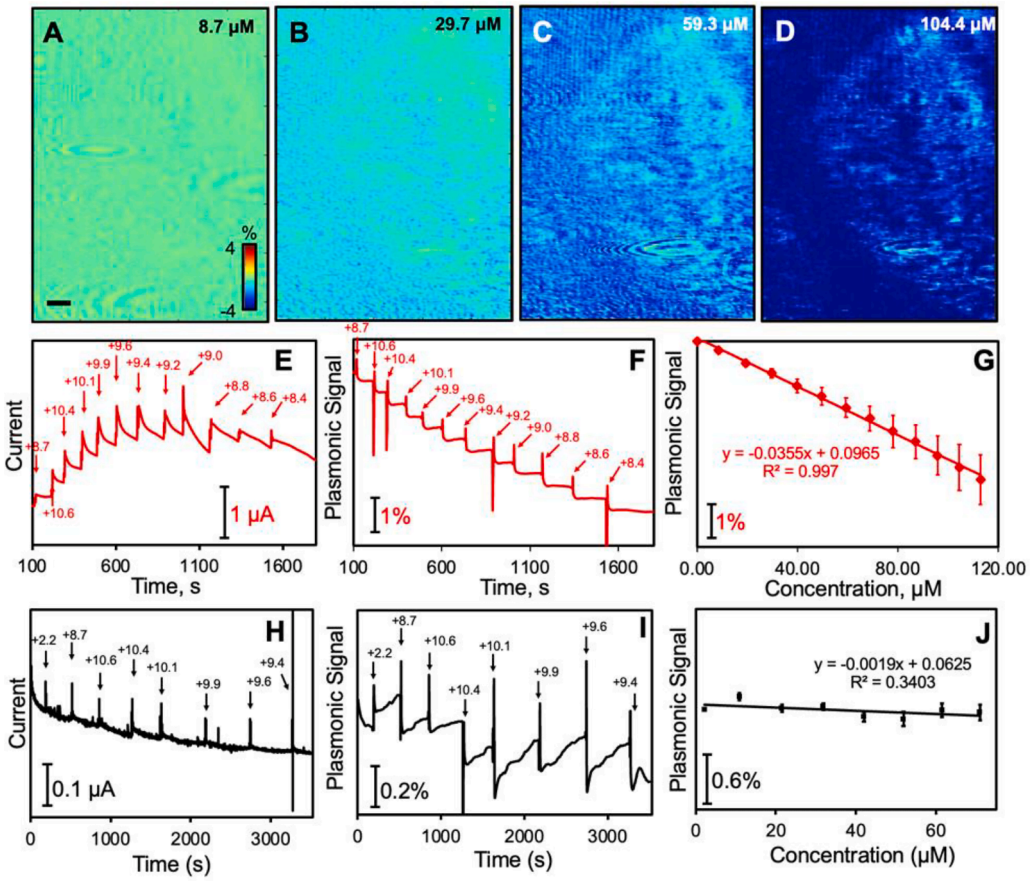

Fig. 2. Amperometric Detection of H_2O_2 Using PB Nanofilm Sensitized-PEM. (A-D) Representative PEM snapshots of the nanofilm upon exposure to varying concentrations of H_2O_2, under a −0.1 V bias. Images were taken before the following injection. Scale bar = 50 μm. (E-J) Concurrent real-time data from the potentiostat (E, H) and PEM (F, I), alongside calibration curves correlating PEM signal intensity with H_2O_2 concentration (G, J), are presented for both a nanofilm-coated sensing chip (E-G) and a bare chip (H-J). In F and I, the PEM signals are averaged over the entire imaged area (600 μm × 450 μm, 0.27 mm^2), while G and J incorporate data as mean ± standard deviation from 88 regions of interest (ROIs) within the imaged area. Each ROI is approximately 54 μm × 54 μm. Numbers in E, F, H, and I indicate the new addition of H_2O_2 in the concentration of μM taking into consideration the dilution factors.

the red profile was extracted from the area labeled by the red dashed line in Fig. S4B. A particle binding event is visible as a bright tail around 464 s. Around 904 s (Fig. S4C), another much larger impurity—possibly an air bubble—appeared and caused an interference in the real-time PEM recording shown in Fig. S4A. However, once the impurity left the location, the PEM recording returned to normal. Overall, the red and black profiles show nearly the same level of signal dependence on H_2O_2 concentrations, demonstrating that the impurities only temporarily interfere with the signal and do not cause a sustainable impact on the sensitivity. We also acknowledge the non-uniformity of the PB sensor (Fig. 2A–D) and its increasing standard deviation towards high concentrations (Fig. 2G). We are currently exploring film synthesis alternatives, including chemical and electrochemical deposition, to achieve a more uniform coating. While these developments are promising for the future refinement of our sensor technology, a comprehensive exploration of these synthesis methods is outside this manuscript's purview and will be detailed in upcoming studies.

3.3. *Spatially resolved detection of locally delivered H_2O_2*

A micromanipulator system was employed to precisely control a 10 μm diameter H_2O_2-containing micropipette. This setup facilitated the formation of a localized concentration gradient on the sensor surface. Figs. 3A–E show concentration heatmaps of the sensor surface during an amperometry recording while the micropipette was actively approaching the sensor surface. These heatmaps, generated by calibrating the original plasmonic signals to H_2O_2 concentrations using the calibration curve equation established in Fig. 2G, captured the emergence and growth of the concentration gradient as the micropipette approached. The alignment of this gradient with the bright field image post-approach (Fig. 3F) validates the real-time tracking capabilities of our system.

Real-time concentration variations during the approach were extracted from selected locations marked in Fig. 3E (dashed circles) and depicted in Fig. 3G. Notably, the red area within the deposition spot showed a significant increase in H_2O_2 concentration as the micropipette drew nearer, confirming the effective delivery of H_2O_2. Some fluctuations in signal were observed, likely due to micropipette holder instability, particularly as the micropipette was near the surface. The smaller concentration changes in the green area and the lack of change in the black area provide solid proof of our technique's ability to map concentrations spatially.

Concentration profile analyses across the delivery site (Fig. 3H) reveal a clear buildup of H_2O_2 as the micropipette moved incrementally closer to the sensor. Further, concentration profiles at a fixed micropipette-to-sensor distance but averaged over varying pixel counts (pixel size of approximately 1 μm × 1 μm), illustrated that detectable concentration gradients were achieved even at the smallest analyzed pixel size (Fig. 3I) with a signal-to-noise ratio (S/N) of 1.8. With the smoothing from five pixels, the S/N can be improved to 6.2. Other post-data processing methods such as frequency domain filtering and Fourier transform can be applied to improve the S/N at a single pixel. This promising detail suggests that, although the current instrument's

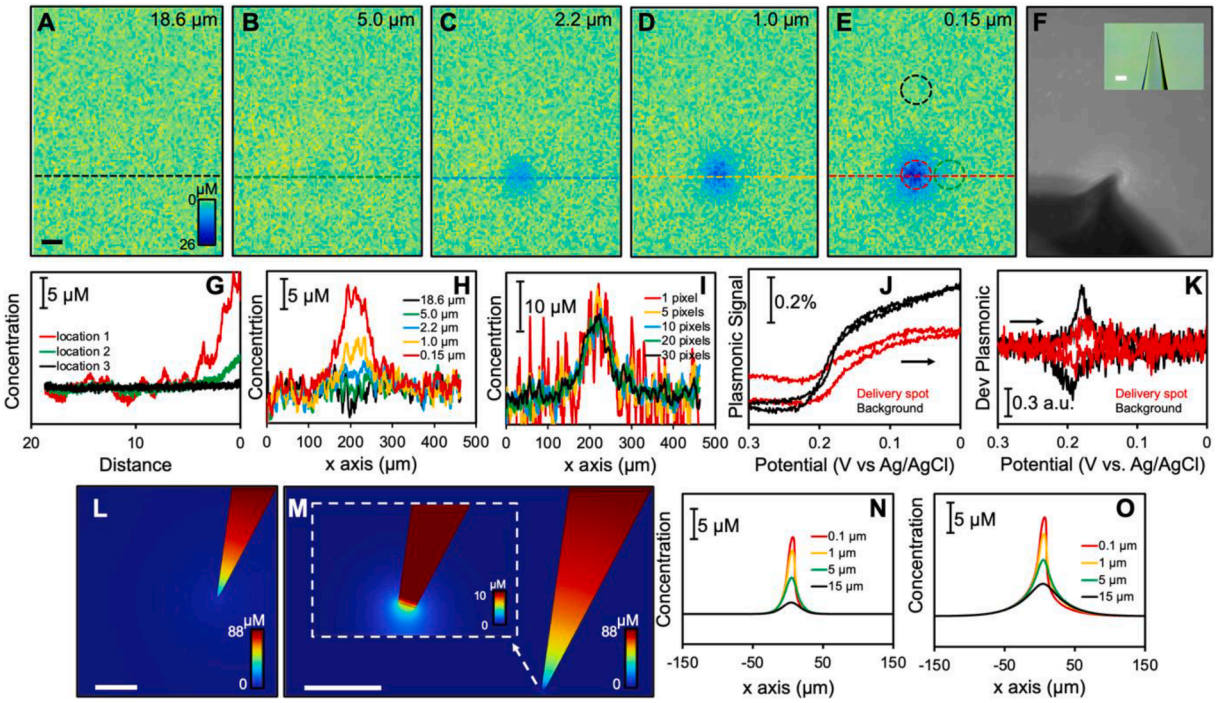

Fig. 3. Spatially Resolved Detection of Locally Delivered H_2O_2 Using PB Nanofilm Sensitized PEM. (A-E) Heatmaps displaying H_2O_2 concentrations at the sensing surface, captured during progressive micropipette approaches under a −0.1 V bias. Scale bar = 50 µm. Concentrations were determined using the calibration equation derived from Fig. 2. (F) Optical image highlighting the micropipette's position post-approach. The inset of F is the optical image of the pipette before usage with a scale bar of 20 µm. (G) Distance-dependent concentration traces from specific ROIs designated with dashed circles in E. (H) Concentration distribution profiles along the x-axis across the site of delivery extracted from A-E, as labelled by the colored dashed lines, for varying micropipette-to-sensor distances, with each data point representing an average over a 20-pixel span (~20 µm) along the y-axis. (I) Concentration distribution profiles along the x-axis at a constant micropipette-to-sensor distance of 0.15 µm as labelled in E, averaged over differing pixel counts along the y-axis. (J, K) Comparative plasmonic cyclic voltammograms at the delivery spot (red) and an unaffected background area (black), shown both prior to (J) and following taking the time derivative of the plasmonic signal (K). (L-O) COMSOL-simulated concentration profiles: (L, M) 2D spatial distribution of H_2O_2 diffusion from the micropipette at distances far from (L) and near to (M) the sensor surface, scale bar = 50 µm; (N, O) Longitudinal concentration profiles across the site of delivery at various micropipette-to-sensor distances, captured at 0.1 s (N) and 1 second (O) after loading the micropipette at the corresponding distances with a pre-set concentration gradient inside.

resolution is limited to 1 µm, an upgrade to a high numerical aperture objective could enable diffraction-limited resolution down to 200 nm [7, 12], with post-processing potentially pushing this beyond the optical diffraction limit [37]. On the other hand, the current temporal resolution is about 20 ms, determined by the frame rate of the camera. A increased rate can be achieved by using a faster camera.

In an alternative setup without an applied bias (data not shown), the absence of contrast at the expected delivery site corroborated that our detection relied on electrochemical conversion between PB and PW rather than refractive index changes due to H_2O_2 concentration differences. Cyclic voltammograms (CVs) conducted with the micropipette in proximity are displayed in Figs. 3J and K. Both of the plasmonic signals increased during the forward CV scan due to the conversion of PB to PW (Fig. 3J), however, the delivery spot (red) established a smaller increase in signal compared to the background spot (black), aligning with the hypothesis that the presence of H_2O_2 leads to the conversion of PW back to PB and a lower net refractive index change [21,38]. This was further demonstrated by a smaller peak height in the post derivative data (Fig. 3K).

To demonstrate the accuracy of experimental results, we utilized COMSOL Multiphysics to simulate H_2O_2 diffusion from the micropipette to the substrate. This simulation was conducted in two phases. The first phase was to assess the depletion of H_2O_2 within the pipette over a minute to mirror the experimental conditions before the micropipette's approach (Fig. 3L). The concentrations derived from this phase provided the baseline for subsequent simulations of H_2O_2 diffusion during the pipette approach. An instance of this diffusion at 15 µm, 0.1 s post-distance attainment, is illustrated in Fig. 3M. Here, the inset shows the H_2O_2 concentration adjacent to the pipette tip, amplified by narrowing the scale of data presentation for enhanced clarity. Figs. 3N and O plot the spatial concentration distributions on the substrate at two distinct timeframes: at 0.1 s and at 1.0 s after distance engagement. Remarkably, the simulated concentration values align with the experimental data presented in Fig. 3H, bolstering the validity of our experimental approach. It is noteworthy, however, that some slight discrepancies between the simulated and experimental outcomes are observed. These may be ascribed to the simulation parameters diverging minimally from the in-experiment conditions. For instance, the pipette-to-substrate distances recorded during experimental runs were estimated relative to the presumed zero-point position of the micropipette, which could introduce a minor, sub-micrometer scale variance.

4. Conclusions

In conclusion, we successfully developed and implemented a new PB nanofilm-sensitized PEM technique that precisely detects hydrogen peroxide (H_2O_2) in a spatially resolved manner. The annealing of PB onto the sensing chip created a nanofilm that exhibited a proportional relationship between the plasmonic signal and the concentration of H_2O_2, validated in amperometric mode. The integration of a micromanipulator system facilitated the localized delivery of H_2O_2, enabling us to map out concentrations at the micrometer scale with remarkable detail. The accuracy of translating PEM signal intensities into reliable concentration measurements has been confirmed through thorough experimental testing and is supported by simulations. Our technique's precision allows us to effectively discern and explore localized activity.

With Prussian blue's proven efficacy in catalyzing dopamine, our method shows substantial potential for propelling research in single-cell exocytosis using dopamine as a model [39,40]. This work not only broadens the applications of PB-sensitized PEM but also signals a step forward in the domain of electrochemical sensing, holding significant promise for future bioanalytical applications.

CRediT authorship contribution statement

Adaly Garcia: Writing – review & editing, Writing – original draft, Visualization, Methodology, Investigation, Formal analysis, Data curation. **Christina Dhoj:** Writing – review & editing, Writing – original draft, Methodology, Investigation. **Samuel Groysman:** Writing – review & editing, Writing – original draft, Visualization, Software, Methodology, Formal analysis, Data curation. **Kinsley Wang:** Software, Formal analysis. **Stellina Ao:** Software, Formal analysis. **Aimee Anguiano:** Investigation. **Tony Tran:** Investigation. **Dianlu Jiang:** Methodology. **Yixian Wang:** Writing – review & editing, Writing – original draft, Visualization, Validation, Supervision, Software, Resources, Project administration, Methodology, Investigation, Funding acquisition, Formal analysis, Data curation, Conceptualization.

Declaration of competing interest

The authors declare that they have no known competing financial interests or personal relationships that could have appeared to influence the work reported in this paper.

Data availability

Data will be made available on request.

Acknowledgments

This work was supported by the National Science Foundation (NSF CHE 2045839, YW, AG, SG ; DMR-1523588, KW) and the National Institutes of Health (NIH R15 NS120157, CD).

This work has also been partially supported by NSF CREST Award (HRD-2112554). S.A., A.A. and T.T. were the recipient of a CREST-CATSUS fellowship, for which we are grateful.

Supplementary materials

Supplementary material associated with this article can be found, in the online version, at doi:10.1016/j.snr.2024.100218.

References

[1] Y. Wang, X. Shan, N. Tao, Emerging tools for studying single entity electrochemistry, Faraday Dis. 193 (2016) 9–39, https://doi.org/10.1039/C6FD00180G.
[2] Y. Yu, T. Sun, M.V. Mirkin, Scanning electrochemical microscopy of single spherical nanoparticles: theory and particle size evaluation, Anal. Chem. 87 (14) (2015) 7446–7453, https://doi.org/10.1021/acs.analchem.5b01690. Jul.
[3] J.L. Fernández, C. Hurth, A.J. Bard, Scanning electrochemical microscopy #54. Application to the study of heterogeneous catalytic reactionsshydrogen peroxide decomposition, J. Phys. Chem. B 109 (2005) 9532–9539, https://doi.org/10.1021/jp050340.
[4] M. Choi, et al., Probing single-particle electrocatalytic activity at facet-controlled gold nanocrystals, Nano Lett. 20 (2) (2020) 1233–1239, https://doi.org/10.1021/acs.nanolett.9b04640. Feb.
[5] N. Ebejer, M. Schnippering, A.W. Colburn, M.A. Edwards, P.R. Unwin, Localized high resolution electrochemistry and multifunctional imaging : scanning electrochemical cell microscopy, Anal. Chem. 82 (2010) 9141–9145.
[6] P. Chen, et al., Spatiotemporal catalytic dynamics within single nanocatalysts revealed by single-molecule microscopy, Chem. Soc. Rev. 43 (4) (2014) 1107–1117, https://doi.org/10.1039/c3cs60215j.
[7] X. Shan, et al., Imaging the electrocatalytic activity of single nanoparticles, Nat. Nanotechnol. 7 (10) (2012) 668–672, https://doi.org/10.1038/nnano.2012.134. Aug.
[8] C.P. Byers, B.S. Hoener, W.-S. Chang, S. Link, C.F. Landes, Single-particle plasmon voltammetry (spPV) for detecting anion adsorption, Nano Lett. 16 (4) (2016) 2314–2321, https://doi.org/10.1021/acs.nanolett.5b04990. Apr.
[9] D. Kurouski, M. Mattei, R.P. Van Duyne, Probing redox reactions at the nanoscale with electrochemical tip-enhanced Raman spectroscopy, Nano Lett. 15 (12) (2015) 7956–7962, https://doi.org/10.1021/acs.nanolett.5b04177.
[10] A.G. Fallis, Handbook of Surface Plasmon Resonance, 53, Royal Society of Chemistry, Cambridge, 2017 [Online]. Available, http://ebook.rsc.org/?DOI=10.1039/9781847558220.
[11] A. Chieng, M. Chiang, K. Triloges, M. Chang, Y. Wang, Recent progress in the studies of electrochemical interfaces by surface plasmon resonance spectroscopy and microscopy, Curr. Opin. Electrochem. 13 (2019) 94–99, https://doi.org/10.1016/j.coelec.2018.11.002. Feb.
[12] Y. Wang, X. Shan, H. Wang, S. Wang, N. Tao, Plasmonic Imaging of Surface Electrochemical Reactions of Single Gold Nanowires, J. Am. Chem. Soc. 139 (4) (2017) 1376–1379, https://doi.org/10.1021/jacs.6b10693. Feb.
[13] S. Nizamov, O. Kasian, V.M. Mirsky, Individual detection and electrochemically assisted identification of adsorbed nanoparticles by using surface plasmon microscopy, Angew. Chem. Int. Ed. 55 (25) (2016) 7247–7251, https://doi.org/10.1002/anie.201600853. Jun.
[14] S. Wang, S. Boussaad, S. Wong, N.J. Tao, High-sensitivity stark spectroscopy obtained by surface plasmon resonance measurement, Anal. Chem. 72 (17) (2000) 4003–4008, https://doi.org/10.1021/ac000504f. Sep.
[15] P. Zhai, J. Guo, J. Xiang, F. Zhou, Electrochemical surface plasmon resonance spectroscopy at bilayered silver/gold films, J. Phys. Chem. C 111 (2) (2007) 981–986, https://doi.org/10.1021/jp065525d.
[16] K.J. Foley, X. Shan, N.J. Tao, Surface impedance imaging technique, Anal. Chem. 80 (13) (2008) 5146–5151, https://doi.org/10.1021/Ac800361p.
[17] S. Wang, X. Huang, X. Shan, K.J. Foley, N. Tao, Electrochemical surface Plasmon resonance: basic formalism and experimental validation, Anal. Chem. 82 (3) (2010) 935–941, https://doi.org/10.1021/ac902178f. Feb.
[18] X. Shan, U. Patel, S. Wang, R. Iglesias, N. Tao, Imaging local electrochemical current via surface plasmon resonance, Science 327 (5971) (2010) 1363. LP–1366Mar.
[19] B. Huang, F. Yu, R.N. Zare, Surface plasmon resonance imaging using a high numerical aperture microscope objective, Anal. Chem. 79 (7) (2007) 2979–2983, https://doi.org/10.1021/Ac062284x.
[20] Y. Fang, et al., Plasmonic imaging of electrochemical reactions of single nanoparticles, Acc. Chem. Res. 49 (11) (2016) 2614–2624, https://doi.org/10.1021/acs.accounts.6b00348. Nov.
[21] A. Garcia, et al., Plasmonic imaging of electrochemical reactions at individual prussian blue nanoparticles, Front. Chem. 9 (September) (2021) 1–11, https://doi.org/10.3389/fchem.2021.718666. Sep.
[22] A. Garcia, S. Wang, N. Tao, X. Shan, Y. Wang, Plasmonic imaging of oxidation and reduction of single gold nanoparticles and their surface structural dynamics, ACS Sens. 6 (2) (2021) 502–507, https://doi.org/10.1021/acssensors.0c02055. Feb.
[23] B. Halliwell, M.V. Clement, L.H. Long, Hydrogen peroxide in the human body, FEBS Lett 486 (1) (2000) 10–13, https://doi.org/10.1016/S0014-5793(00)02197-9. Dec.
[24] C. Lennicke, J. Rahn, R. Lichtenfels, L.A. Wessjohann, B. Seliger, Hydrogen peroxide – production, fate and role in redox signaling of tumor cells, Cell Commun. Signal. 13 (1) (2015) 39, https://doi.org/10.1186/s12964-015-0118-6. Dec.
[25] H. Sies, Hydrogen peroxide as a central redox signaling molecule in physiological oxidative stress: oxidative eustress, Redox Biol. 11 (2017) 613–619, https://doi.org/10.1016/j.redox.2016.12.035. Apr.
[26] S. Urban, et al., Multiparametric, spatially resolved detection of H_2O_2 and O_2 with electrochemical microsensor array in synthesis membrane microreactors, in: 2019 20th International Conference on Solid-State Sensors, Actuators and Microsystems & Eurosensors XXXIII (TRANSDUCERS & EUROSENSORS XXXIII), IEEE, Berlin, Germany, 2019, pp. 1297–1300, https://doi.org/10.1109/TRANSDUCERS.2019.8808261. Jun.
[27] M.A. O'Connell, J.R. Lewis, A.J. Wain, Electrochemical imaging of hydrogen peroxide generation at individual gold nanoparticles, Chem. Commun. 51 (51) (2015) 10314–10317, https://doi.org/10.1039/c5cc01640a.
[28] H. Guo, H. Aleyasin, B.C. Dickinson, R.E. Haskew-Layton, R.R. Ratan, Recent advances in hydrogen peroxide imaging for biological applications, Cell Biosci. 4 (1) (2014) 64, https://doi.org/10.1186/2045-3701-4-64. Dec.
[29] Y. Zuo, Y. Jiao, C. Ma, C. Duan, A novel fluorescent probe for hydrogen peroxide and its application in bio-imaging, Molecules 26 (11) (2021) 3352, https://doi.org/10.3390/molecules26113352. Jun.
[30] M.A. Komkova, A.A. Zarochintsev, E.E. Karyakina, A.A. Karyakin, Electrochemical and sensing properties of Prussian Blue based nanozymes 'artificial peroxidase, J. Electroanal. Chem. 872 (2020) 114048, https://doi.org/10.1016/j.jelechem.2020.114048. Sep.
[31] Y. Miao, J. Chen, X. Wu, K. Fang, A. Jia, J. Liu, Immobilization of Prussian blue nanoparticles onto Thiol SAM Modified Au electrodes for electroanalytical or biosensor applications, J. Nanosci. Nanotechnol. 7 (8) (2007) 2877–2882, https://doi.org/10.1166/jnn.2007.672. Aug.
[32] J.D. Qiu, H.Z. Peng, R.P. Liang, J. Li, X.H. Xia, Synthesis, characterization, and immobilization of Prussian blue-modified au nanoparticles: application to electrocatalytic reduction of H2O2, Langmuir 23 (4) (2007) 2133–2137, https://doi.org/10.1021/la062788q.
[33] S.A. Agnihotry, P. Singh, A.G. Joshi, D.P. Singh, K.N. Sood, S.M. Shivaprasad, Electrodeposited Prussian blue films: annealing effect, Electrochim. Acta 51 (20) (2006) 4291–4301, https://doi.org/10.1016/j.electacta.2005.12.008. May.

[34] C.-C. Chen, Y. Zhou, L. a. Baker, Scanning ion conductance microscopy, Annu. Rev. Anal. Chem. 5 (1) (2012) 207–228, https://doi.org/10.1146/annurev-anchem-062011-143203. Jul.
[35] P.S. Stewart, G.A. McFeters, C.-T. Huang, Biofilm control by antimicrobial agents, in: J.D. Bryers (Ed.), Biofilms II: Process Analysis and Applications, Wiley, New York, 2000, pp. 373–405. Wiley series in ecological and applied microbiology.
[36] P.J. Kulesza, M.A. Malik, A. Denca, J. Strojek, In situ FT-IR/ATR spectroelectrochemistry of Prussian Blue in the solid state, Anal. Chem. 68 (14) (1996) 2442–2446, https://doi.org/10.1021/ac950380k. Jan.
[37] Y. Wang, T. Yuan, H. Su, K. Zhou, L. Yin, W. Wang, A Bubble-STORM approach for super-resolved imaging of nucleation sites in hydrogen evolution reactions, ACS Sens. (2020), https://doi.org/10.1021/acssensors.0c01293 p. acssensors.0c01293Aug.
[38] D. Jiang, L. Sun, T. Liu, W. Wang, Thin-film electrochemistry of single Prussian Blue nanoparticles revealed by surface Plasmon resonance microscopy, Anal. Chem. 89 (21) (2017) 11641–11647, https://doi.org/10.1021/acs.analchem.7b03061. Nov.
[39] P. Pandey, B. Upadhyay, Studies on differential sensing of dopamine at the surface of chemically sensitized ormosil-modified electrodes, Talanta 67 (5) (2005) 997–1006, https://doi.org/10.1016/j.talanta.2005.04.030. Oct.
[40] S. Yang, J. Zhao, S. Tricard, L. Yu, J. Fang, A sensitive and selective electrochemical sensor based on N, P-Doped molybdenum Carbide@Carbon/Prussian blue/graphite felt composite electrode for the detection of dopamine, Anal. Chim. Acta 1094 (2020) 80–89, https://doi.org/10.1016/j.aca.2019.09.077. Jan.